

# カメラ応答関数の自動校正を伴う 照度差ステレオ：非ランバート物体への拡張

モンコンマーン ウィーンナー<sup>1,a)</sup> 岡部 孝弘<sup>1,b)</sup> 佐藤 洋一<sup>1,c)</sup>

**概要：**従来、照度差ステレオなどの明るさ解析では、線形のカメラ応答関数を仮定していたために、事前にカメラ応答関数を校正したり、線形の応答関数を持つ特殊なカメラを利用したりする必要があった。これに対して我々は、カメラ応答関数の自動校正を伴う照度差ステレオを提案している。しかしながら、我々の従来手法は、ランバート物体を仮定しているために、鏡面反射を生じるような非ランバート物体に適用することが出来なかった。そこで本研究では、未知かつ非線形な応答関数を持つカメラで撮影された画像から、非ランバート物体の法線とカメラ応答関数を同時に推定する手法を提案する。本研究の基本的な着想は、いわゆるロバスト推定の枠組みに基づいて、鏡面反射成分などを外れ値として扱うことにある。実画像を用いた実験を行い、カメラ応答関数が未知かつ非線形であっても、提案手法が非ランバート物体の法線を頑健に推定出来ることを確認した。

## 1. Introduction

Photometric stereo is a technique to estimate surface orientations of a static object from a set of images captured by a fixed camera [12]. It assumes the object follows Lambertian reflectance model, illuminated by known varying light sources. A number of techniques have been developed to overcome such assumptions and allow photometric stereo in more general circumstances, unknown light sources and non-Lambertian surfaces.

Another common assumption that often presumed in the computer vision algorithms, include photometric stereo, is input images must be captured by a camera with linear response function, *i.e.* the image intensity is proportional to the irradiance received by the camera sensor. Unfortunately, the response functions of the consumer cameras are generally nonlinear and unknown. Moreover, a camera setting such as white balance affects the response function. Therefore, the radiometric calibration is required to be preprocessed to cancel the effect of nonlinear response function before the images can be used in any physics-based analysis of the scene. We proposed a photometric stereo with auto-radiometric calibration technique by exploiting data that inhere in the photometric stereo images to recover the response function [8]. However, this technique assumes an object with Lambertian reflection property so the estimated shape and response function are distorted by specular highlights observed in non-Lambertian surfaces. Moreover, we cannot directly apply the specular detection techniques to this case because of nonlinear response function.

In this paper, we propose an auto-radiometric calibration photometric stereo technique for non-Lambertian surface. Because

many non-Lambertian surfaces behave like Lambertian surface at the area with no highlight, we can treat a highlight pixel as an outlier which deviates from the Lambert model. Therefore, it would be possible to simultaneously estimate the shape of a non-Lambertian surface and the response function of a camera by incorporating what so-called robust estimation techniques such as RANSAC [2] into the auto-radiometric calibration technique. We conducted a number of experiments to demonstrate that our proposed method can accurately estimate the shape of given objects with non-Lambertian surface and the response function regardless of its nonlinearity.

The contribution of this work is to achieve an auto-radiometric calibration in photometric stereo technique that can handle non-Lambertian surface. Our method requires neither radiometric calibration nor additional images for the calibration; it allows photometric stereo for more real-world materials, *e.g.* ceramics, and plastics. The shape estimation can be performed without worrying about the nonlinearity of the response function in a camera.

The rest of this paper is organized as following. Section 2 briefly describes the related works. A photometric stereo method to simultaneously recover surface normals of a non-Lambertian object and an inverse response function is explained in Section 3. The experimental results are shown in Section 4 followed by conclusion remarks in Section 5.

## 2. Related Works

This work relates to radiometric calibration and specular removal. The most widely used technique for radiometric calibration was proposed by Mitsunaga and Nayar [7]. They make use of multiple images taken with different known exposure times. The ratios between pixel intensity and exposure time are used to estimate a response function. However, this method requires a lot of additional images and considered time-consuming. Shi *et al*

<sup>1</sup> 東京大学生産技術研究所

<sup>a)</sup> wiennat@iis.u-tokyo.ac.jp

<sup>b)</sup> takahiro@iis.u-tokyo.ac.jp

<sup>c)</sup> ysato@iis.u-tokyo.ac.jp

[11] proposed a radiometric calibration technique that uses input images for color photometric stereo. This method makes use of the linearity of RGB color in the same pixel along an input image set to estimate a response function. However, this method cannot recover the response function from a gray object and cannot be used with grayscale input images. Mongkulmann *et al* [8] proposed an auto radiometric calibration method for grayscale photometric stereo. This method estimates surface normals and response function simultaneously using consistency between irradiance calculated from response function and irradiance calculated from surface property. However, it requires specular-free input images. Thus, we cannot apply this technique to a non-Lambertian object without the removal of specular component first. Otherwise, the estimated response function is distorted by specularity.

To solve specular problem in photometric stereo, one can regard specular pixel as an outlier and exclude it from surface estimation. Coleman and Jain [6] took this approach and proposed a photometric stereo technique for non-Lambertian surface using four light sources. They estimated four candidate albedos at a certain location from four possible triplets selected from four light sources. If all of the candidate albedos do not consistent, it is because of specularity. The smallest albedo is used for surface estimation. Barsky and Petrou [1] modified this method to detect both highlights and shadows by using temporal pixel intensity and linear dependency. Unfortunately, these techniques assume input images are captured by a camera with linear response function. Therefore, we cannot directly apply these methods as an individual step before the automatic response function technique due to the nonlinearity of response function.

Our proposed method extends the Mongkulmann's photometric stereo framework [8] to handle a non-Lambertian surface. Unlike the previous work, our proposed method avoids using specular pixel intensities in the estimation by integrating what so-called robust estimation such as RANSAC [2] to determine specular region and estimate response function at the same time. RANSAC has been used by several works to handle specular highlights in face recognition task [10] and to remove specularity from non-Lambertian surfaces in photometric stereo [5] [4]. Mukaigawa *et al* [9] uses RANSAC to classify diffuse and specular region using images taken under different light sources.

### 3. Proposed Method

#### 3.1 Conventional Photometric Stereo

Firstly, we briefly explain the classic photometric stereo method [12]. It assumes a target object follows the Lambertian model illuminated under varying directional light sources. The irradiance at the point  $p$  observed under the  $d$ -th directional light source is represented as

$$E_{pd} = \mathbf{l}_d \mathbf{n}_p, \quad (1)$$

where  $\mathbf{n}_p$  denotes the normal vector at the point  $p$  scaled by its albedo and  $\mathbf{l}_d$  denotes the  $d$ -th light source direction scaled by its intensity ( $d = 1, 2, \dots, D$ ). Conventionally, eq.(1) can be expressed in the matrix form as

$$\begin{pmatrix} E_{p1} \\ \vdots \\ E_{pD} \end{pmatrix} = \begin{pmatrix} l_{1x} & l_{1y} & l_{1z} \\ \vdots & \vdots & \vdots \\ l_{Dx} & l_{Dy} & l_{Dz} \end{pmatrix} \begin{pmatrix} n_{px} \\ n_{py} \\ n_{pz} \end{pmatrix},$$

$$\mathbf{E}_p = \mathbf{L} \mathbf{n}_p, \quad (2)$$

where  $\mathbf{l}_d = (l_{dx}, l_{dy}, l_{dz})^T$  and  $\mathbf{n}_p = (n_{px}, n_{py}, n_{pz})^T$ .

Given light source directions and intensities are known, the surface normals and its albedo can be estimated from at least three images by least square method:

$$\hat{\mathbf{n}}_p = (\mathbf{L}^T \mathbf{L})^{-1} \mathbf{L}^T \mathbf{E}_p. \quad (3)$$

This is equivalent to

$$\hat{\mathbf{n}}_p = \arg \min_{\mathbf{n}_p} \sum_{d=1}^D (E_{pd} - \mathbf{n}_p^T \mathbf{l}_d)^2. \quad (4)$$

The surface normal and albedo are computed from the estimated scaled surface normal  $\hat{\mathbf{n}}_p$  as  $\hat{\mathbf{n}}_p / |\hat{\mathbf{n}}_p|$  and  $|\hat{\mathbf{n}}_p|$  respectively.

#### 3.2 Simultaneous Estimation of Surface Normals and Inverse Response Function

We briefly explain a photometric stereo technique for estimating surface normals and inverse response function at the same time. The radiometric response function  $f$  maps an irradiance  $E$  to a pixel intensity  $I$ . Because response function is a monotonic increasing function, we can find an inverse function  $g = f^{-1}$  which maps a pixel intensity back to its corresponding irradiance. We normalize the range of irradiance and pixel intensity to  $[0, 1]$  without loss of generality.

We assume the inverse response function  $g$  can be represented as  $K$ -degree polynomials similar to [7],

$$E = g(I) = \sum_{k=0}^K c_k I^k, \quad (5)$$

where  $c_k$  is the coefficient of the  $k$ -th polynomial. With boundary condition  $E(0) = 0$  and  $E(1) = \sum_{k=0}^K c_k = 1$ , we can derive the relationship between irradiance  $E$  and pixel intensity  $I$  as,

$$\begin{aligned} E &= c_1 I + \sum_{k=2}^K c_k I^k, \\ &= I + \sum_{k=2}^K c_k (I^k - I). \end{aligned} \quad (6)$$

Then, we can formulate a linear least square problem to find the appropriate surface normals and the coefficients

$$\begin{aligned} (\{\hat{\mathbf{n}}_p\}, \{\hat{c}_k\}) &= \arg \min_{(\{\mathbf{n}_p\}, \{c_k\})} \\ &\sum_{p=1}^P \sum_{d=1}^D \left[ E_{pd} - \mathbf{n}_p^T \mathbf{E}_d + \sum_{k=2}^K c_k (E_{pd}^k - I_{pd}) \right]^2, \end{aligned} \quad (7)$$

subjects to the monotonicity constraint,

$$\sum_{k=2}^K c_k (1 - k I^{k-1}) < 1. \quad (8)$$

when  $E > 0$ .

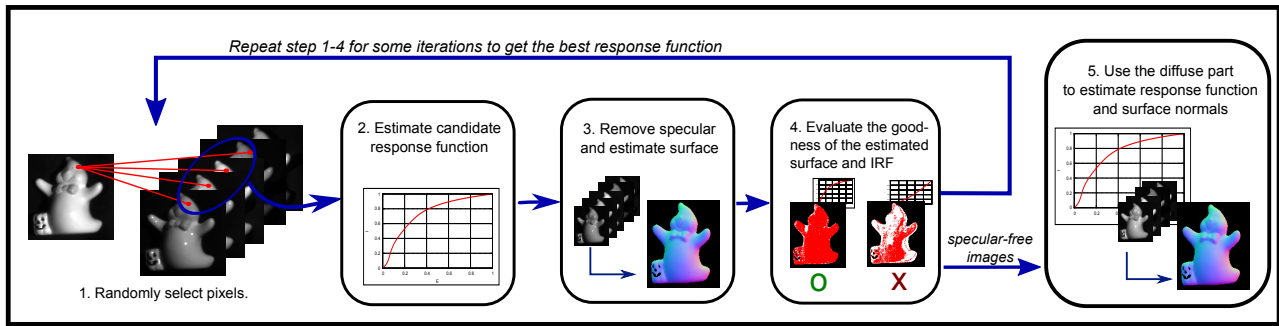


**Fig. 1** The overview of our proposed method: (1)  $s$  random pixels are sampled.  $t$  pixel intensities from each sampled pixel are used. (2) Inverse response function is estimated and the input images are calibrated using the estimated function. (3) Specular regions are detected and removed. The diffuse pixels are considered inliers. (4) The estimated response function and the estimated shape are evaluated. Step 1-4 are repeated for some iterations to obtain the best specular-free images. (5) The specular-free images are used to estimate response function and shape.

### 3.3 Extension for Non-Lambertian Surface

This subsection explains the method to handle specularly observed on non-Lambertian surface.

We iteratively estimate the response function and surface normals. In each iteration,  $s$  random pixels are sampled and  $t$  pixel values from each sampled pixel are selected. Then, the selected pixel values are used to estimate a candidate inverse response function and the input images are radiometrically calibrated using the estimated function. Here, we assume the response function is accurately estimated so we perform specular removal at this step to extract the diffuse regions. Then, the diffuse regions are used to estimate surface normals. The accuracy of the estimated response function is evaluated to consider the one that matches the input images the best. Finally, the diffuse areas from the iteration with the best response function are used to reestimate the response function and surface normals.

The detailed algorithms are given as following.

#### Step 1. Pixels Random Selection

We select a number of pixel values to estimate a candidate inverse response function. Given the whole set of images are affected by the same response function, we can use only a small subset of pixel intensities to estimate the response function. Let  $K$  denotes the degree of polynomials. Firstly,  $s$  pixels are randomly selected. Then, the number of required pixel intensities  $t$  for a selected pixel  $p$  is determined. Since there are 3 unknowns for surface normals for each pixel selected, namely  $n_{px}$ ,  $n_{py}$ , and  $n_{pz}$ , plus  $K - 1$  unknowns for the coefficients of inverse response function, therefore  $t$  can be written as,

$$t = \left\lceil \frac{3 \times s + K - 1}{s} \right\rceil. \quad (9)$$

For each selected pixel,  $t$  pixel intensities from the same pixel along the set of images are randomly selected.

Although we did not mention for the sake of simplicity, shadows and saturated pixel intensities are removed from the estimation by thresholding. The pixels which have number of pixel intensities less than three after the removal are also excluded from the selection.

#### Step 2. Estimation of a Candidate Inverse Response Function

A candidate inverse response function  $g$  is estimated using the

selected pixel intensities. If all of the selected pixel intensities do not consist of specular component, we can determine an inverse response function with eq.(7) subjects to the constraint eq.(8). Then, the input images are mapped by the estimated inverse response function  $g$  into the irradiance  $E^{\text{observed}}$ .

#### Step 3. Specular Region Detection and Removal

The specular regions are detected and removed in this step. We utilize a simple pixel intensity comparison which is similar to the one in Barsky [1]. Given specular region is observed within some limited light directions, we can regards a specular pixel intensity as an outlier that does not satisfy the Lambertian model. We apply RANSAC here to iteratively determine the largest subset of pixel intensities that do not contain specularity. Then the appropriate surface normals is estimated from the diffuse pixel intensities.

Assume that the set of images is radiometrically calibrated and converted into their corresponding irradiance  $E$ . For each point  $p$ , three irradiance values,  $E_{pi}$ ,  $E_{pj}$ , and  $E_{pk}$  where  $1 \leq i, j, k \leq D$ , are randomly selected. If the selected irradiance values contain only diffuse component, this becomes the classic photometric stereo case. A unique surface normals  $n_p$  can be determined by eq.(4). Consequently, we can estimate the irradiance  $E_{pd}^{\text{estimated}}$  from the  $d$ -th light source  $l_d$  and the estimated surface normals  $n_p$ ; the estimated irradiance must be equals to its corresponding observed irradiance  $E_{pd}^{\text{observed}}$ . On the other hand, if the selected irradiance values contain a specular component, the estimated surface normals becomes distorted and the  $E_{pd}^{\text{estimated}}$  becomes inconsistent to the  $E_{pd}^{\text{observed}}$ . Therefore we measure the goodness of the estimated surface normals by the number of inliers whose estimated irradiance equals to the observed one. The irradiance  $E_{pd}^{\text{observed}}$  is considered an inlier if following condition is satisfied,

$$|E_{pd}^{\text{estimated}} - E_{pd}^{\text{observed}}| \leq \tau_s E_{pd}^{\text{observed}}, \quad (10)$$

where  $\tau_s$  is a threshold.

The combinations of three irradiance values,  $E_{pi}$ ,  $E_{pj}$ , and  $E_{pk}$ , are selected iteratively to obtain a distribution of surface normals. Then, the surface normals  $n_p$  is estimated from the inliers of the iteration with highest number of inliers. The specular detection and surface estimation are performed on every foreground pixel to acquire the surface normals  $n$ .

#### Step 4 Evaluation of the Candidate Inverse Response Function

The accuracy of the estimated inverse response function is evaluated. If the inverse response function  $g$  and the surface normals  $\mathbf{n}$  are accurately estimated, the irradiance  $E^{\text{observed}}$  which mapped by the inverse response  $g$  must consistent with the irradiance calculated from the surface property. Hence, we calculate the irradiance  $E^{\text{estimated}}$  with the surface normals  $\mathbf{n}$ . We determine the supporting inliers with the same criterion to the specular detection. The irradiance  $E_{dp}^{\text{observed}}$  supports the estimated inverse response function if it satisfies eq.(10).

The step 1 to 4 are repeated for many iterations to get a numbers of candidate inverse response functions. The inliers for the inverse response function with the largest number of supports are considered diffuse pixel intensities by consensus.

#### Step 5 Estimation of the response function and surface shape

In this step, the diffuse pixels are used to estimate the inverse response function and the surface normals. The eq.(7) and (8) are used once again to reestimate the coefficients of the inverse response function  $\hat{c}_k$  and the surface normals  $\hat{\mathbf{n}}$  from the diffuse pixel intensities.

### 4. Experiments

We verify our proposed by experiments using both synthetic images and real objects. We used MATLAB implementation of the trust region reflective quadratic programming for the optimization. We decide the number of iterations for surface estimation and response function estimation as suggested in Fischler[2],

$$\text{number of iterations} = \left\lceil \frac{\log(1 - \rho)}{\log(1 - w^n)} \right\rceil, \quad (11)$$

where  $\rho$  is probability that all selected pixel intensities are inliers at least once,  $w$  is probability that a selected pixel intensity is an inlier and  $n$  denotes sampling size. we set  $w = 0.8$  empirically and  $n = ts$  for the estimation of response function, we set  $w = 3/D$  and  $n = 3$  for the specular detection. We set  $\rho = 0.99$ ,  $\tau = 0.06$ ,  $s = 1$ , and degree of polynomials  $K = 6$  are selected empirically for both synthetic images and real objects cases.

#### 4.1 Synthetic Images

We evaluate the performance of our proposed method by comparing the result with that of the classic photometric stereo[12] and result from auto-radiometric calibration photometric stereo for Lambertian surface[8] using synthetic images. The synthetic images were a sphere with uniform albedo and specular factor. We randomly picked ten light directions around the object. We applied two response functions, namely agfa-scala-200xCDSStandard1 and agfapan-apx-400CD, from the DoRF database[3] to the rendered images to emulate the effect of non-linear response function.

Figure 4 shows the color coded normal map for the ground truth (a), the estimated ones from our proposed method (b), the estimated ones from the auto-radiometric calibration photometric stereo without specular detection (d), and the estimated ones from classic photometric stereo (f). Although the estimated surface from the auto-radiometric calibration photometric stereo without

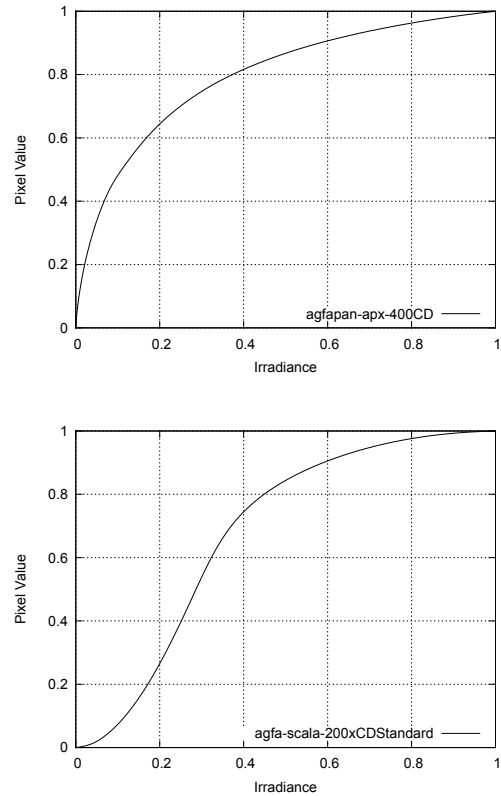


Fig. 2 Response functions used in the experiments. (top) Agfapan-apx-400CD (bottom) Agfa-scala-200xCDSStandard

specular detection is similar to the ground truth, the distorted areas due to specularity can be easily spotted in the disparity map (e). Figure 5 shows the result from the images taken with a different response function.

We plotted the estimated inverse response function in Figure 6. The plotted function and RMS error were computed using the pixels with intensities less than the ninetieth percentile of the largest pixel intensities. This is because the number of bright diffuse pixels is small due to specularity so the estimated function where the pixel intensity is near 1 cannot be constrained well and therefore is not accurate. Moreover, the error propagates to the scale of the estimated response function because we formulate the relationship between irradiance and pixel intensity with the boundary condition  $E(0) = 0$  and  $E(1) = 1$ . Therefore, our algorithm has a kind of ambiguity in the scale of the estimated response function. This ambiguity does not affect the estimated surface normals but it affects the overall scale of the estimated albedos instead.

Table 1 shows quantitative results: the average of the angular error of estimated normals maps compared to the ground truth, and the root mean square error of the scaled estimated functions to the compared to the ground truth. The errors from our method are decreased as there is no distortion due to specularity. The root mean square errors show that our method can accurately estimate the shape of the inverse radiometric response function.

#### 4.2 Real Images

We evaluate the performance of our proposed method by comparing the result with that of the classic photometric stereo[12] and result from auto-radiometric calibration photometric stereo

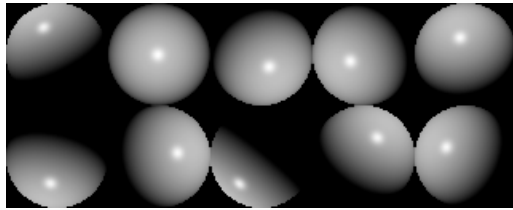


Fig. 3 Synthetic images: Sphere

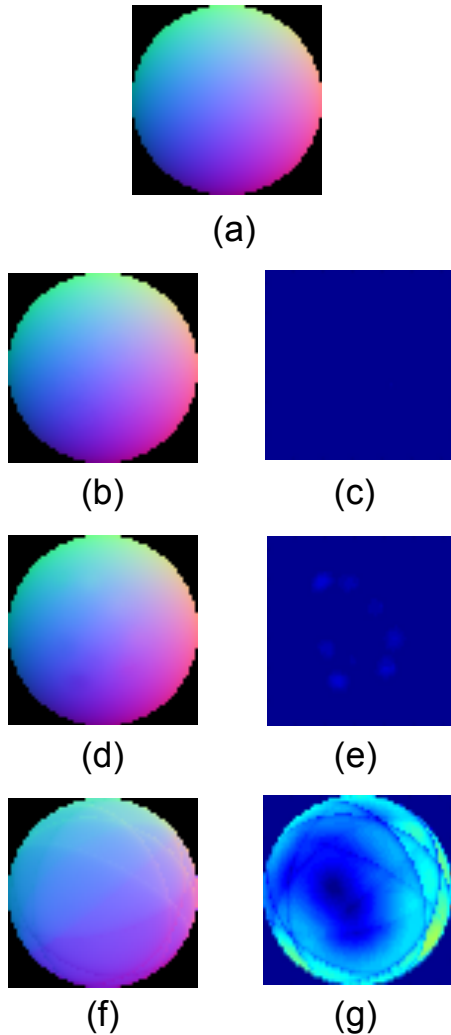


Fig. 4 Estimated normal maps of the synthetic images: sphere (agfapan). (a) the ground truth, (b) normals map from our proposed method and its different to ground truth, (d) normals map from the auto-radiometric calibration photometric stereo without specular removal, (f) normals map from the classic photometric stereo. (c) (e) (g) show angular difference of the estimated normal maps to the ground truth.

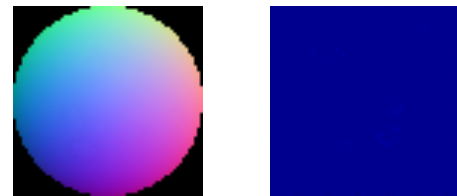
Table 1 Estimation results for the synthetic sphere. Average of the angular error of estimated normal map, and the RMS error of estimated response function.

|                   | Surface normal (classic) | Surface normal (auto-calib.) | Surface normal (ours) | Inverse response function |
|-------------------|--------------------------|------------------------------|-----------------------|---------------------------|
| Sphere(agfapan)   | 15.3°                    | 0.6°                         | <b>0.2°</b>           | 0.001                     |
| Sphere(agfascala) | 4.24°                    | 0.7°                         | <b>0.3°</b>           | 0.004                     |

for Lambertian surface[8] using the images of real objects. The target objects are TOMATO, and FISH. They are made of shiny plastic, and ceramic with glossy paint respectively. We captured 20 images of the objects by a Point Grey's Flea camera with two nonlinear response functions, namely, agfa-scala-

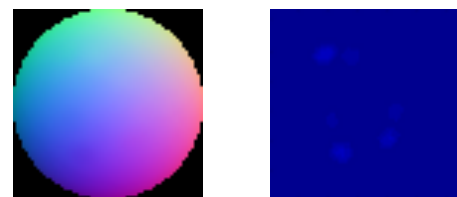


(a)



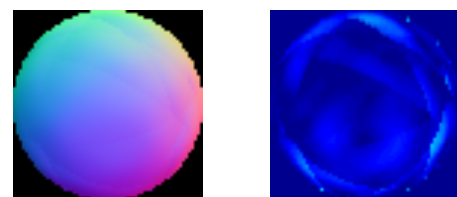
(b)

(c)



(d)

(e)



(f)

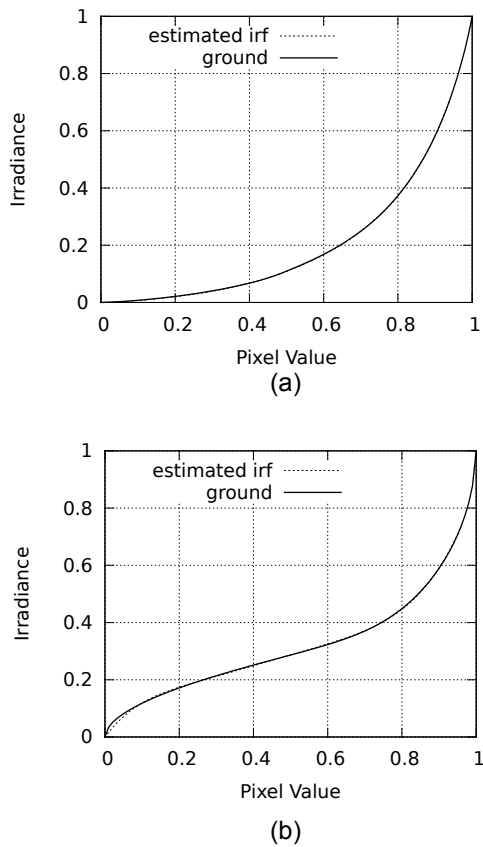
(g)

Fig. 5 Estimated normal maps of the synthetic images: sphere (agfascala).

200xCDSstandard and agfapan-apx-400CD. We computed the ground truth by using classic photometric stereo with specular removal on the images captured with a linear response function.

Same as the synthetic images, we show the color coded normal map for our proposed method, the auto-radiometric calibration photometric stereo with no outlier removal, and the classic photometric stereo method. Our proposed method can remove the specular regions and estimate the surface shape that similar to the ground truth. Moreover, the shadows and holes in the bottom part of FISH were removed correctly (figure 10). The edge of the hole is accurately estimated compared to the result from classic photometric stereo (f) and the auto-radiometric calibration photometric stereo (d). In addition, our proposed method can estimate the inverse response functions that are similar to the ground truth (fig. 12). Similar to the experiments with synthetic images, the estimated functions contain a kind of ambiguity in scale.

Table 2 shows quantitative results: the average of the angular error of estimated normals maps compared to the ground truth, and the root mean square error of the scaled estimated functions. Similar to the experiments with synthetic images, the angular errors slightly decreased for our proposed method compared to the auto-radiometric calibration photometric stereo without out-



**Fig. 6** Estimated inverse response function. The graph is plotted using the first ninetyth percentile of pixel intensities. (a) agfapan-apx-400CD (b) agfa-scala-200xCDStandard.

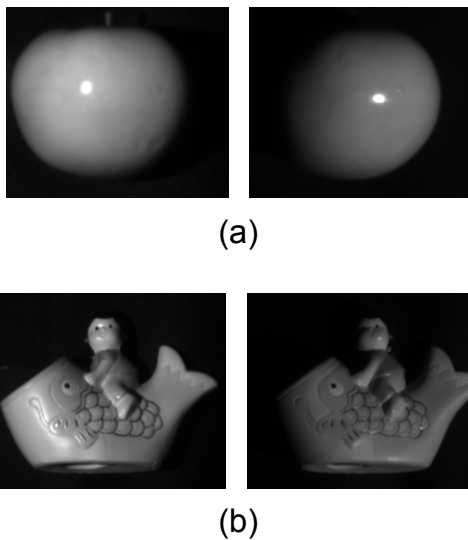


**Fig. 7** Real images: (a) TOMATO (b) FISH

**Table 2** Estimation results for the real images sphere when  $\tau_s = 0.6$ . Average of the angular error of estimated normal map, and the RMS error of estimated response function.

|                   | Surface normal (classic) | Surface normal (auto-calib.) | Surface normal (ours) | Inverse response function |
|-------------------|--------------------------|------------------------------|-----------------------|---------------------------|
| FISH(agfapan)     | 17.90°                   | 3.89°                        | <b>2.22°</b>          | 0.0063                    |
| FISH(agfascala)   | 6.91°                    | 3.13°                        | <b>2.40°</b>          | 0.0055                    |
| TOMATO(agfapan)   | 17.90°                   | 2.77°                        | <b>1.80°</b>          | 0.0075                    |
| TOMATO(agfascala) | 5.56°                    | 1.76°                        | <b>1.69°</b>          | 0.0086                    |

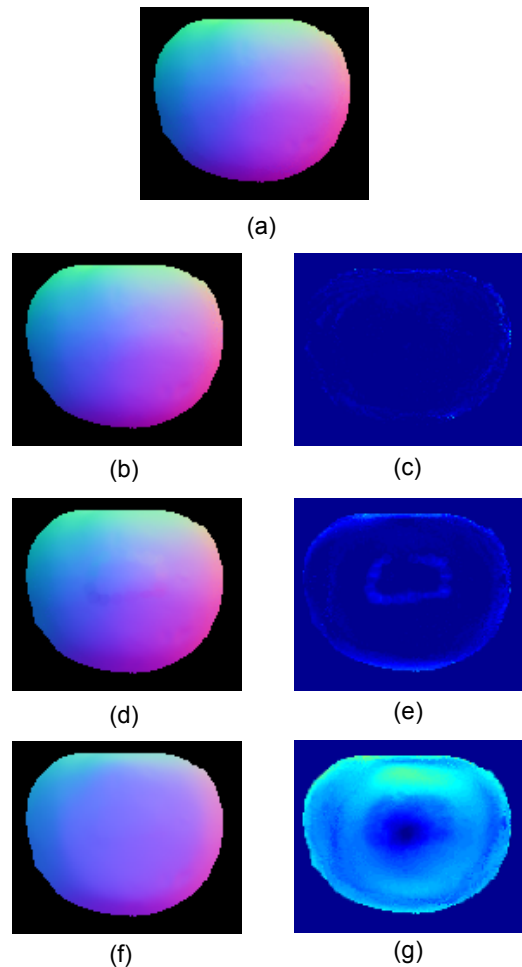


**Fig. 8** Estimated normal maps of the real images: TOMATO (agfapan).

lier removal. The root mean square errors show that our proposed method can estimate the shape of the inverse response function accurately despite the observed intensities do not cover the whole range of intensities.

## 5. Conclusion and Future Work

This paper presents an extension of photometric stereo with auto-radiometric calibration for non-Lambertian surface. We utilize RANSAC to integrate the specular detection technique to the auto-radiometric calibration framework for photometric stereo. Our proposed method allows surface modeling, response function estimation and outlier removal to be performed at the same time. We experimentally show that our method can detect specular region and estimate the surface orientation accurately even though the input images are captured by a camera with nonlinear response function.

As for the future work, an extension for the unknown light sources situation is still remain to be addressed.

## References

- [1] Barsky, S. and Petrou, M.: The 4-source photometric stereo technique for three-dimensional surfaces in the presence of highlights and shadows, *Pattern Analysis and Machine Intelligence, IEEE Transactions on*, Vol. 25, No. 10, pp. 1239 – 1252 (online), DOI: 10.1109/TPAMI.2003.1233898 (2003).
- [2] Fischler, M. A. and Bolles, R. C.: Random sample consensus: a paradigm for model fitting with applications to image analysis and

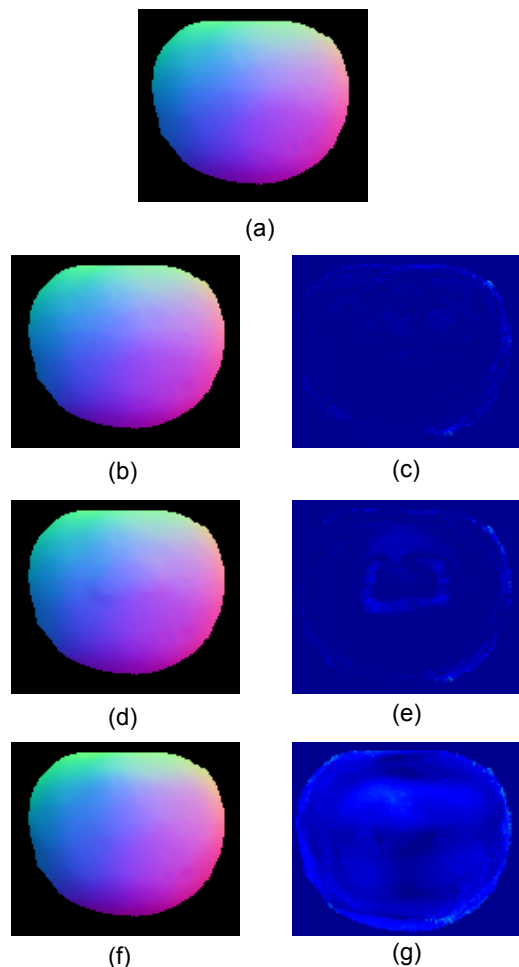


Fig. 9 Estimated normal maps of the real images: TOMATO (agfascala).

automated cartography, *Commun. ACM*, Vol. 24, No. 6, pp. 381–395 (online), DOI: 10.1145/358669.358692 (1981).

- [3] Grossberg, M. and Nayar, S.: Determining the camera response from images: what is knowable?, *IEEE Trans. PAMI*, Vol. 25, No. 11, pp. 1455–1467 (2003).
- [4] Higo, T., Miyazaki, D. and Ikeuchi, K.: Multi-View Photometric Stereo using Rough Shape Data Application for Estimation of Reection Parameters, *Proc. MIRU 2008*, pp. 1280–1287 (2008).
- [5] Holroyd, M., Lawrence, J., Humphreys, G. and Zickler, T.: A photometric approach for estimating normals and tangents, *ACM Trans. Graph.*, Vol. 27, No. 5, pp. 133:1–133:9 (online), DOI: 10.1145/1409060.1409086 (2008).
- [6] Jr., E. N. C. and Jain, R.: Obtaining 3-dimensional shape of textured and specular surfaces using four-source photometry, *Computer Graphics and Image Processing*, Vol. 18, No. 4, pp. 309 – 328 (online), DOI: 10.1016/0146-664X(82)90001-6 (1982).
- [7] Mitsunaga, T. and Nayar, S.: Radiometric self calibration, *Proc. CVPR '99*, pp. 374–380 (1999).
- [8] Mongkulmann, W., Okabe, T. and Sato, Y.: Photometric stereo with auto-radiometric calibration, *Computer Vision Workshops (ICCV Workshops), 2011 IEEE International Conference on*, pp. 753 –758 (online), DOI: 10.1109/ICCVW.2011.6130328 (2011).
- [9] Mukaigawa, Y., Ishii, Y. and Shakunaga, T.: Analysis of photometric factors based on photometric linearization, *J. Opt. Soc. Am. A*, Vol. 24, No. 10, pp. 3326–3334 (online), DOI: 10.1364/JOSAA.24.003326 (2007).
- [10] Okabe, T. and Sato, Y.: Object recognition based on photometric alignment using RANSAC, *Computer Vision and Pattern Recognition, 2003. Proceedings. 2003 IEEE Computer Society Conference on*, Vol. 1, pp. I–221 – I–228 vol.1 (online), DOI: 10.1109/CVPR.2003.1211357 (2003).
- [11] Shi, B., Matsushita, Y., Wei, Y., Xu, C. and Tan, P.: Self-calibrating photometric stereo, *Proc. CVPR2010*, pp. pp.1118–1125 (2010).
- [12] Woodham, R.: Photometric method for determining surface orientation from multiple images, *Optical Engineering*, Vol. 19, No. 1, pp. 139–144 (1980).

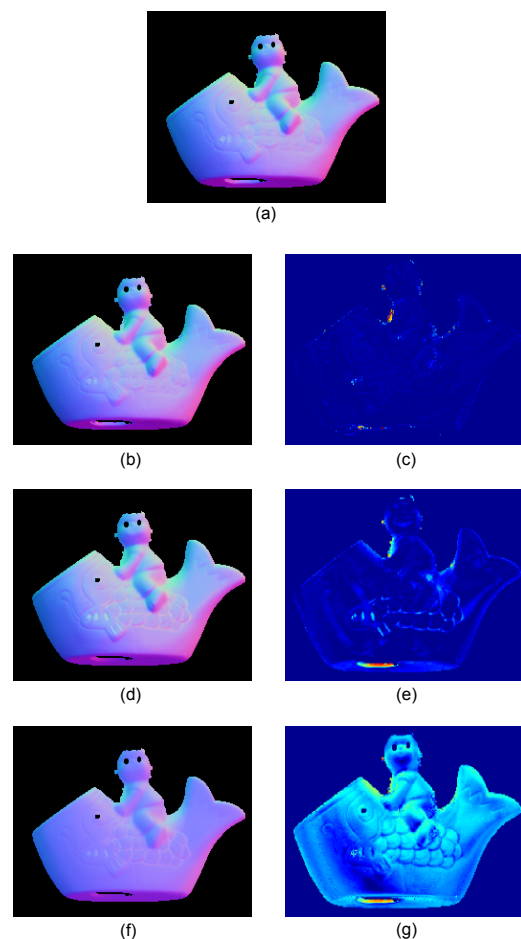


Fig. 10 Estimated normal maps of the real images: FISH (agfapan).

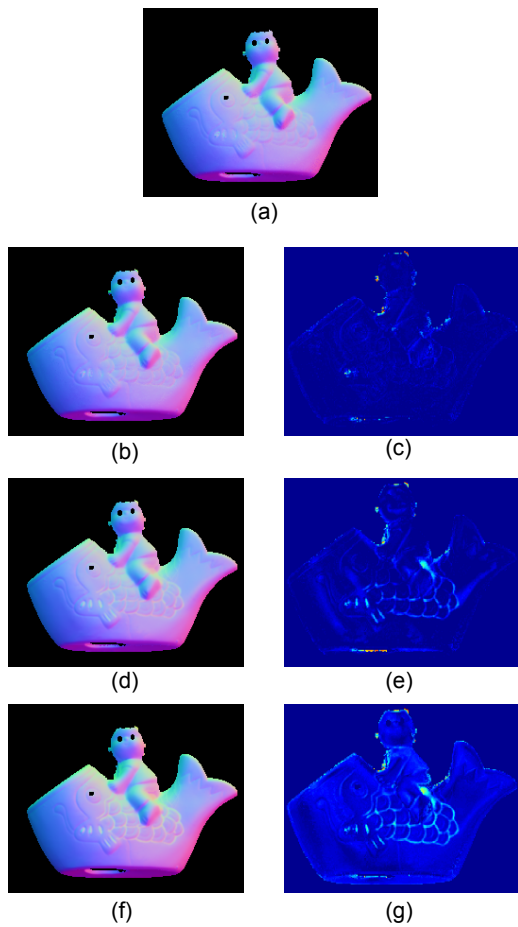


Fig. 11 Estimated normal maps of the real images: FISH (agfascala).

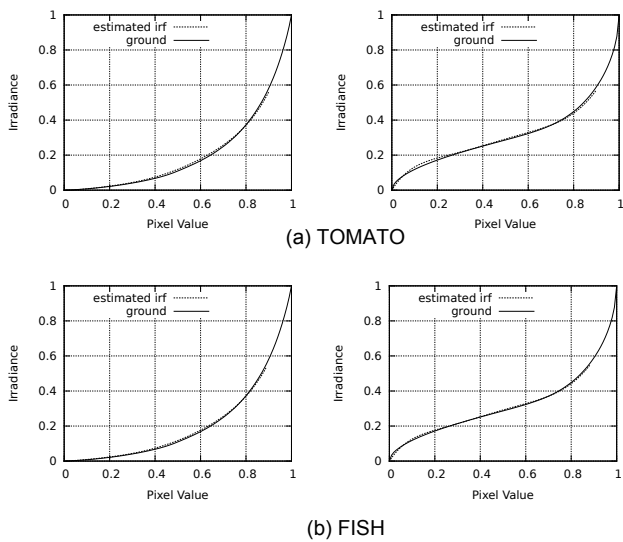


Fig. 12 The estimated response functions for TOMATO and FISH.